

# Monte Carlo validation of optimal material discrimination using spectral x-ray imaging

S. J. Nik,<sup>1</sup> R. S. Thing,<sup>2</sup> R. Watts,<sup>3</sup> T. Dale,<sup>4</sup> B. Currie,<sup>5</sup> and J. Meyer<sup>6</sup>

<sup>1</sup>*Department of Physics and Astronomy,  
University of Canterbury, Christchurch, New Zealand.*

<sup>2</sup>*Institute of Clinical Research, University of Southern Denmark, Odense, Denmark.*

<sup>3</sup>*UVM MRI Center for Biomedical Imaging,  
University of Vermont College of Medicine, Burlington, VT, USA.*

<sup>4</sup>*BlueFern, University of Canterbury, Christchurch, New Zealand.*

<sup>5</sup>*Medical Physics and Bioengineering Department,  
Christchurch Hospital, Christchurch, New Zealand.*

<sup>6</sup>*Department of Radiation Oncology,  
University of Washington Medical Center, Seattle, WA, USA.*

## Abstract

The aim of this work was to develop a framework to validate an algorithm for determination of optimal material discrimination in spectral x-ray imaging. Using Monte Carlo (MC) simulations based on the BEAMnrc package, material decomposition was performed on the projection images of phantoms containing up to three materials. The simulated projection data was first decomposed into material basis images by minimizing the z-score between expected and simulated counts. Statistical analysis was performed for the pixels within the region-of-interest consisting of contrast material(s) in the MC simulations. With the consideration of scattered radiation and a realistic scanning geometry, the theoretical optima of energy bin borders provided by the algorithm were shown to have an accuracy of  $\pm 2$  keV for the decomposition of 2 and 3 materials. Finally, the signal-to-noise ratio predicted by the theoretical model was also validated. The counts per pixel needed for achieving a specific imaging aim can therefore be estimated using the validated model.

PACS numbers: 07.05.Tp,87.57.C-,87.59.-e

## I. INTRODUCTION

With the ability of acquiring multiple energy resolved images in a single acquisition, spectral CT imaging can be considered an expansion of dual energy CT. Photon counting detectors (PCDs) with energy discriminating abilities, such as the Medipix and XPAD detectors, have been built to achieve this [1, 2]. Energy discriminating PCDs are equipped with tunable pulse height discriminators within the electronics of the PCDs. Modern photon counting detectors are often equipped with several independent discriminators, with as many as 8 provided in the Medipix3 detectors [2, 3]. Data associated with a higher energy level can be subtracted from that of a lower energy to form data for an energy bin [4].

Based upon Alvarez and Macovski's [5] technique of dual-energy imaging, the advent of spectral x-ray imaging has enabled three-component decomposition. Given the projection data, material decomposition can be realized by estimating the thicknesses or the areal densities of specific materials, prior to reconstruction. The benefits of spectral x-ray imaging in material identification have been ubiquitously demonstrated for medical [4, 6, 7] and security applications [8]. Higher numbers of energy bins have been demonstrated to be beneficial in material quantification [9]. For a limited number of bins, the optimal arrangement of energy windows that maximizes the spectral information for material separation remains unclear.

Material decomposition in this work is performed by minimizing the z-score between the measurements and the expected counts given by the Beer-Lambert equation. Based on this approach, a theoretical model of optimizing the spectral information has previously been developed by minimizing the uncertainties of thickness estimates [10]. The focus of this paper is to validate the minimization of confidence regions on material quantities under the influence of Poisson counting noise, scattered radiation and a realistic scanning geometry. The theoretical algorithm was also extended to predict the variances of material thicknesses, which enables the estimation of counts per pixel needed for an optimal material discrimination. A framework of Monte Carlo (MC) simulations for spectral imaging is presented and the previously established material decomposition method was applied on the simulated data to validate the extended theoretical model.

## II. BACKGROUND

The complete formulation of our optimization model for material discrimination by minimizing the z-score has been presented in [10] and will be summarized here briefly.

Consider the linear attenuation coefficients  $\mu_i$  of material  $i$  as a result of Compton (incoherent) scattering and the photoelectric effect. The number of photons,  $N$  between energies  $E_l$  and  $E_h$  after being transmitted through  $i = 1, \dots, m$  materials, as governed by the Beer-Lambert equation is:

$$N(E_l, E_h, \mathbf{t}) = \int_{E_l}^{E_h} N_0(E) e^{-\sum_{i=1}^m \mu_i(E) t_i} dE, \quad (1)$$

where  $N_0$  is the number of incident photons.  $\mathbf{t}$  represents a set of thicknesses  $t_i$  for  $i = 1, \dots, m$  materials.

Given the linear dependency of the material attenuation functions, only two materials can be decomposed, if the imaging object does not present any k-edges within the energies considered [11, 12]. However, a third material with a k-edge within the detected x-ray spectrum can be discriminated with 3 or more spectroscopic measurements. In the regime of spectral x-ray imaging, at least as many bins,  $n$ , as materials have to be fitted for the discrimination of  $m$  materials ( $n \geq m$ ). Henceforth, it is assumed that photons are binned into a minimum of  $n = 2$  energy bins, for the separation of at least  $m = 2$  materials. Photons are allocated into energy bin  $k$  for  $k = 1, \dots, n$ , where  $E_{(l,k)}$  and  $E_{(h,k)}$  are the low and high limits for bin  $k$ , respectively. The photon count in bin  $k$  is denoted  $N_k$ , where  $N_k$  follows a Poisson distribution with a mean of  $\lambda_k$ ; the standard deviation is  $\sigma_k = \sqrt{\lambda_k}$ .

As  $\lambda_k$  is sufficiently large,  $N_k$  can be approximated to a Gaussian distribution. The z-score between the measurements,  $\mathbf{x} = \{x_k\}$ , and the expected counts,  $\boldsymbol{\lambda} = \{\lambda_k\}$ , can therefore be written as

$$z = \frac{\mathbf{x} - \boldsymbol{\lambda}}{\boldsymbol{\sigma}} = \frac{x_1 - \lambda_1}{\sqrt{\lambda_1}} = \frac{x - \lambda}{\sqrt{\lambda}}, \quad (2)$$

for measurements consisting of  $n = 1$  bin. The Mahalanobis distance, which is the z-score for  $n > 1$  energy bins, is given by [10, 13]

$$z = \left\{ \left[ \sum_{k=1}^n \left( x_k - \lambda_k(\mathbf{t}) \right)^2 \times \frac{1}{\lambda_k(\mathbf{t})} \right] \times \frac{1}{n} \right\}^{\frac{1}{2}}, \quad (3)$$

in which a factor of  $1/n$  has been introduced for convenience to negate the dependency of  $z$  on the number of energy bins. Mapping the z-score in the thickness space therefore leads

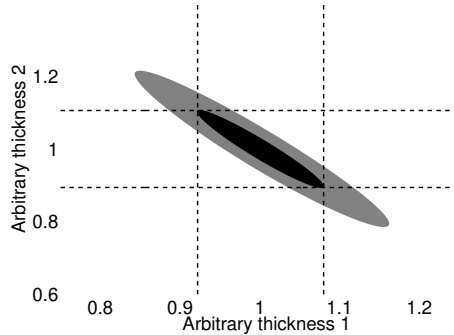


FIG. 1. The black ellipse marks the 63% confidence region formed by a z-score of unity. The outer ellipse represents the confidence region for a z-score of 2 for  $m = 2$  materials, encompassing a probability content of 98%. Expanding this to  $m = 3$  materials results in a confidence volume.

to an elliptical contour plot for  $m = 2$  materials and  $n = 2$  bins, indicating a multivariate normal distribution [13, 14]. A confidence region formed by a z-score of unity is shown as the black ellipse in figure 1, which contains a probability content,  $\beta$ , of 63%. The  $\beta$ -value may be interpreted as meaning that there is a 63% chance that given a measurement  $\mathbf{x}$ , the actual thicknesses would lie within this particular region. Similarly, the 98% confidence region formed by a z-score of 2 is represented by the gray ellipse. Located at the center of the two-dimensional ellipse is a z-score of zero, corresponding to  $\boldsymbol{\tau} = \{\tau_i\}, i = 1, \dots, m$ , where  $\boldsymbol{\tau}$  is the combination of thicknesses that is most consistent with the measurement  $\mathbf{x}$ . The confidence ellipse can be expanded into any higher dimensions e.g. a volume for  $m = 3$  materials [10, 14].

The bounding box of the ellipsoidal confidence region, as depicted in figure 1, enables the calculation of the standard deviations ( $\sigma_i$ ) and correlation coefficient ( $\rho$ ) of the thicknesses for the formation of the covariance matrix of the thickness population,  $V$  [14]:

$$V = \begin{pmatrix} \sigma_1^2 & \rho\sigma_1\sigma_2 & \rho\sigma_1\sigma_3 \\ \rho\sigma_1\sigma_2 & \sigma_2^2 & \rho\sigma_2\sigma_3 \\ \rho\sigma_1\sigma_3 & \rho\sigma_2\sigma_3 & \sigma_3^2 \end{pmatrix}.$$

The diagonal elements in the matrix can be used to quantify the confidence region and thus the uncertainties of the thickness estimates. Given the number of energy bins  $n$ , the objective of the model is to locate the energy thresholds  $E_{(l,k)}$  and  $E_{(h,k)}$  for  $k = 1, \dots, n$  that give the smallest confidence region in the thickness space. This was achieved by an exhaustive search through the space of all possible combinations of energy bins  $E_{(l,k)}$  and

$E_{(h,k)}$  in this paper and in the previous work [10].

### III. METHODS

Despite their promising potential, the performance of PCDs is at present limited by charge sharing [2], scattered radiation [15], finite energy resolution [4] and relatively low read-out speed [6]. To investigate the achievable potential of spectral x-ray imaging, for example, Roessl *et al.* [15] resorted to the ideal environment of CT simulations to investigate the maximum signal to noise ratio (SNR) in the basis images of high atomic number material to bypass the limitations. Other simulations of spectral x-ray imaging have been performed using commercial packages [11, 16, 17], open source packages [9, 18], or analytical methods [19]. We chose a different MC simulation code system, known as BEAMnrc [20, 21], because of its availability, ease of use as well as our previous experience with the system [22, 23]. The BEAMnrc system is based on the EGSnrc code [24] and comes with extensive documentation plus interactive graphical user interfaces. The recognition of the package through publication statistics and a review on the advantages on BEAMnrc over other MC packages was provided by Rogers [25].

#### A. Monte Carlo simulation setup

Using the BEAMnrc MC code system, simulations were carried out on the BlueFern<sup>®</sup> supercomputer at the University of Canterbury, Christchurch, New Zealand. The scanning geometry was set up to correspond to the locally built Medipix All Resolution System (MARS) CT scanner (MARS Bioimaging Ltd, New Zealand), currently customized for biomedical imaging of human specimen and small animal sample [26]. For the x-ray tube, CIRCAPP component module was used to replicate the round exit window and SLABS to include the 1.5mm beryllium and 2.5mm aluminum filtration corresponding to [11]. The 90/10 atomic percent tungsten/rhenium alloy anode target was simulated with the XTUBE component module. The electron beam impinging on the target was simulated as a 120keV monoenergetic, parallel rectangular source energy incident from the side to enable validations of optimal energy bins with the previous work.

The simulation of the scanning system was split into two parts. First the tube housing

was simulated and a phase space (phsp) file scoring the energy, position, direction and interaction history of each particle was recorded. The phsp file immediately at the back of the exit window of the x-ray tube (phsp1) was in turn used as the input to the simulation of particle transport through the imaging object. The source-to-object distance was set to 75mm. A second phsp file (phsp2) was placed at 115mm recording particles reaching the detector plane. Our imaging object was designed using the FLATFILT component module to be a uniform water cylinder containing at least one cylindrical layer of contrast material to allow for decomposition of  $m \geq 2$  materials. The layer(s) of contrast material(s) and the water cylinder had a radius of 3mm and 6mm around the beam axis, respectively. Material thicknesses were defined in section III C to be the same as in [10]. Spaces at the back of the x-ray tube filtration and between the imaging object and the detector plane consisted of air specified by the SLABS component module.

Cross sections including Rayleigh scattering were generated from the XCOM dataset using the PEGS4 code system for all the materials used in this work. Directional bremsstrahlung splitting and photon forcing were used in the x-ray production to improve simulation efficiency. The bremsstrahlung splitting field radius and the source-to-surface distance of the splitting field used were 2.8 cm and 13.5 cm, respectively. NIST bremsstrahlung cross-section data was used. All Monte Carlo simulations were run with  $3 \times 10^8$  primary histories and the cut-off energy was 1keV for both electrons and photons.

One of the main differences between the BEAMnrc simulation and the optimization algorithm described in [10] is the inclusion of scattered radiation. In BEAMnrc, the interaction of each particle with the imaging object was tracked via the LATCH bit identification tag to create additional images/spectra with only primary photons. Particle interactions with the air regions were ignored. Information in the phsp files were decoded particle by particle using an in-house developed Matlab code. The data was organized in a stack of two-dimensional matrices containing particles within 1 keV ranges to allow for retrospective formation of energy-selective images [23]. The spatial variation in the photon counts was corrected by using an open beam image of 1 to 120 keV prior to material decomposition. Spectral distribution, given in photon fluence/keV/incident particles of the simulated phase space file was derived using the BEAM Data Processor (BEAMDP) program [27] distributed with BEAMnrc.

## B. Thickness estimation

The pixelated measurements were binned as input to  $\mathbf{x}$  in (3) for estimation of  $\mathbf{t}$ . Material decomposition was performed pixel-by-pixel using the spectrum scored in phsp2 in a  $128 \times 128$  pixel detector grid of  $220 \times 220 \mu\text{m}^2$  each. A direct way to find the solution for (3) is by mapping a look-up table of counts for an extensive sample of thicknesses. The solution can then be provided by locating the thicknesses that are most consistent with the binned measurements:

$$\mathbf{t} = \arg \min_t \left\{ \left[ \sum_{k=1}^n \left( x_k - \lambda_k(\mathbf{t}) \right)^2 \times \frac{1}{\lambda_k(\mathbf{t})} \right] \times \frac{1}{n} \right\}^{\frac{1}{2}}. \quad (4)$$

The accuracy of the solution given by the look-up table, however, is dependent on the sample size [28] and a huge set of data points may therefore be required for sufficient accuracy. In this work, a more direct approach was realized by implementing an iterative search algorithm, which implements the Nelder-Mead algorithm [29]. This was carried out for both the simulated projection data with and without the inclusion of scattered radiation in the BEAMnrc model. By using the look-up table solution as our initial estimates, the Mahalanobis distance in equation 3 was minimized using the Matlab *fminsearch* function without requiring the likelihood function. Furthermore, the determination of the effective attenuation over an energy range can be avoided [10].

## C. Validation of optimal material discrimination

For a constant x-ray tube voltage and current, the theoretical model in [10] provided a solution of choosing energy bins for spectral imaging based on the smallest confidence region under the influence of Poisson statistics. To reiterate, a limitation of this model is that it does not take into account scattered radiation. To achieve optimal spectrum weighted attenuation difference in discriminating 0.01 cm of iodine and 1.5 cm of water, Nik *et al.* [10] showed that the optimal bin border ( $E_{(h,1)}$ ) is at 60 keV. When  $E_{(h,1)}$  is fixed at the iodine K-edge of 33 keV, the optimal higher bin border ( $E_{(h,2)}$ ) was found to be at 51 keV for the discrimination of iodine, calcium and water.

Using the BEAMnrc framework, projections for an object consisting of  $\tau_I = 0.01$  cm of iodine between two 0.75 cm cylindrical layers of water background ( $\tau_{H_2O} = 1.5$  cm) were simulated. To decompose 3 materials, the projection data of  $\tau_I = 0.01$  cm and  $\tau_{Ca} = 0.22$  cm

stacked between two 0.75 cm cylindrical layers of water background was simulated. The density for iodine and calcium was defined to be the same as in [10], i.e.  $4.93 \text{ g cm}^{-3}$  and  $1.55 \text{ g cm}^{-3}$ , respectively.

For a given incident x-ray spectrum, a pertinent problem is to determine the minimum exposure to achieve an imaging task. The Rose’s criterion [30] of  $\text{SNR} \geq 5$  is often used as a target for image quality (e.g. in [31]). When decomposing a homogenous material  $i$  with thickness  $\tau_i$ , the SNR within the uniform region-of-interest (ROI) can be provided by the ratio of the reference thickness to the standard deviation of thickness population,  $(\tau_i/\sigma_i)$ . Likewise, in estimating the material quantity in a pixel,  $\sigma_i$  represents the uncertainty in the estimation. An imaging task can thus be setup as achieving the  $\tau_i/\sigma_i$  value of 5, in the quantification of thickness  $\tau_i$ , or in the homogenous ROI of the decomposed image  $i$ . The minimum number of photons per unit area required in order to accomplish the imaging task can be subsequently computed to fulfill the ALARA principle [32].

To directly compare with the BEAMnrc MC simulation in this work, however, the image noise was estimated for the simulated detected counts. Using the theoretical model, the image noise was computed as variance ( $\sigma_i^2$ ) as in [15] and [31]. The diagonal elements of the covariance matrix described in section II incorporates  $\sigma_i^2$  and can therefore be utilized for the prediction of image noise (or SNR). This enables a direct comparison between the  $\sigma_i^2$  values obtained from the metric and the simulation. For the discrimination of iodine/water,  $\sigma^2$  was determined at an interval of 1 keV for  $E_{(h,1)}$  ranging from 20 keV to 100 keV, whereas  $E_{(h,1)}$  was fixed at 33 keV and  $\sigma^2$  was computed for  $E_{(h,2)}$  between 36 keV to 100 keV for the discrimination of iodine, calcium and water.

In the BEAMnrc model, the precision of material decomposition was examined by determining the image noise of the material basis images. Mean and variance were computed for the central 690 pixels in the region with contrast material(s). The simulated variance was computed for bin border energies ranging from 20 keV to 100 keV for the decomposition of two materials and 36 keV to 100 keV for the decomposition of three materials, as in the theoretical model. Bin border energies below 20 keV and above 100 keV were considered suboptimal in both models due to photon starvation.

While variance is given by the averaged difference between the thickness output and its mean thickness value, another important measure for material quantification is the averaged difference between the output and the actual value of thicknesses, known as the bias. The



mean square error (MSE) incorporates both the bias and variance. The following figure of merit (FOM) was therefore formulated as a validation of the theoretical model in [10]:

$$\text{FOM} = \left( \sum_{i=1}^m \text{MSE}_i / \tau_i^2 \right)^{-\frac{1}{2}}. \quad (5)$$

(5) was evaluated for bin border energies ( $E_{(h,1)}$ ) from 20 keV to 100 keV for the decomposition of iodine and water. For the decomposition of 3 materials, the lower bin border energy ( $E_{(h,1)}$ ) was held at the K-edge of iodine (33 keV), while a FOM curve was plotted for the upper bin border energies ( $E_{(h,2)}$ ) ranging from 36 keV to 100 keV for the higher energy bin to validate the results in [10].

## IV. RESULTS

### A. Validation of optimal material discrimination

A representative projection image in figure 2(a) shows two concentric circular regions. The darker inner region (i) shows the pixels with higher attenuation due to the contrast material(s) within the water cylinder and the outer mid-gray region (ii) represents the water region without contrast material. While decomposition was performed on the full-field projections, only the ROI with the overlapping contrast materials (region i) was analyzed.

Figure 3 shows a representative set of material basis projection images decomposed using equation 4. A quantitative measurement of the decomposition's precision and accuracy is summarized in figures 4 and 5. The solid line represents the mean thickness over the 690 pixels within region (i) in figure 2(a), whereas the error bars show the standard deviation ( $\sigma$ ) for the decomposition using a particular bin border energy. The reference thicknesses ( $\tau_i$ ) is plotted with dotted lines to provide an indication of the bias of the decomposition.

The variance ( $\sigma^2$ ) and the MSE are tabulated in table I to show the consistency with the estimated image noise given by the theoretical model described in section II. Specifically, the theoretical variance ( $\text{variance}_A$ ), the simulated variance ( $\text{variance}_B$ ) and the MSE were averaged over the 5 keV around the theoretical optimal bin border energy, i.e. optimal  $E_{(h,1)} \pm 2$  keV and optimal  $E_{(h,2)} \pm 2$  keV for the decomposition of two and three materials, respectively. The minimal bias around the optimal bin border was reflected in the similar MSE and variance values for the decomposition of two materials. Note that some bin border

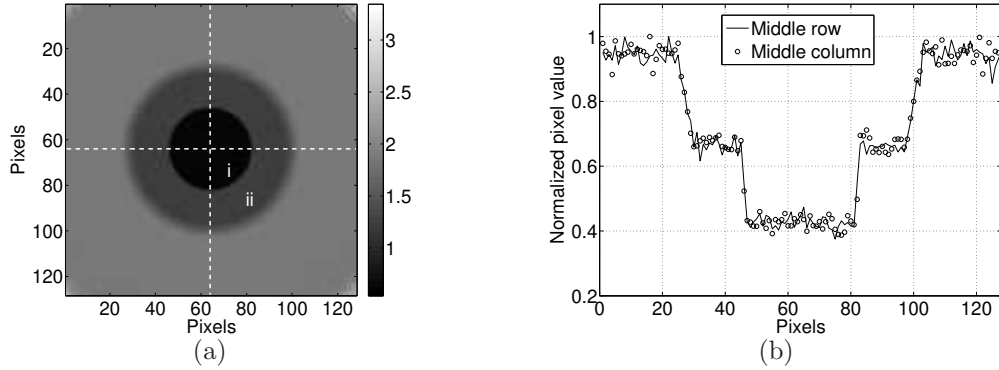


FIG. 2. A representative (a) projection image and (b) set of profiles upon normalization using the open beam image. Color bar in (a) indicates an arbitrary unit upon normalization. The inner (region i) and outer (region ii) concentric circular regions are the ROIs with and without contrast material(s) within the water cylinder, respectively. Statistical analysis was performed on the pixels within the region i. (b) The profile across the horizontal axis (solid line) is relatively constant and is used as a reference to show no reminiscence of the Heel effect in the corrected middle column profile (circles) after normalization against the open beam.

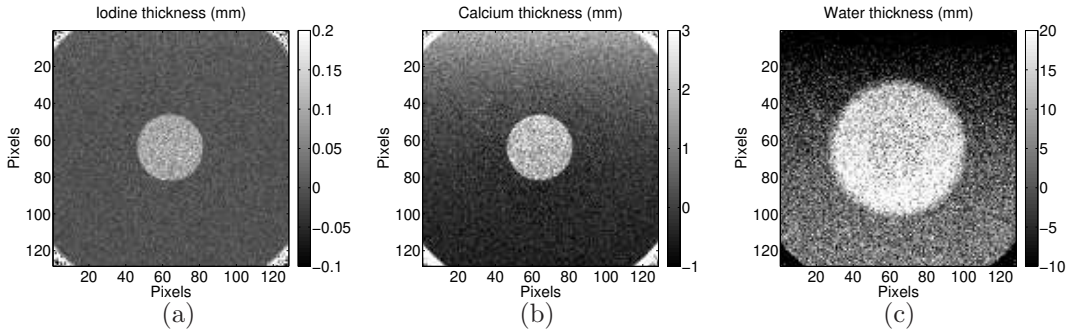


FIG. 3. The decomposed material basis images of (a) iodine, (b) calcium and (c) water. A quantitative analysis of the accuracy as well as the precision can be found in figure 6, figure 7 and table I.

energies, e.g. 28 keV for the decomposition of iodine/water in figure 4, provided inaccurate material thicknesses (see section V).

For the case of three materials (figure 5), a higher MSE compared to the variance, particularly for the calcium image, was obtained without the rejection of scattered radiation. This can be seen in the deviation of the solid line from  $\tau_{Ca}$  in figure 5(b). Figure 5(e) shows a considerable reduction in the bias of thickness estimation for calcium upon rejection of

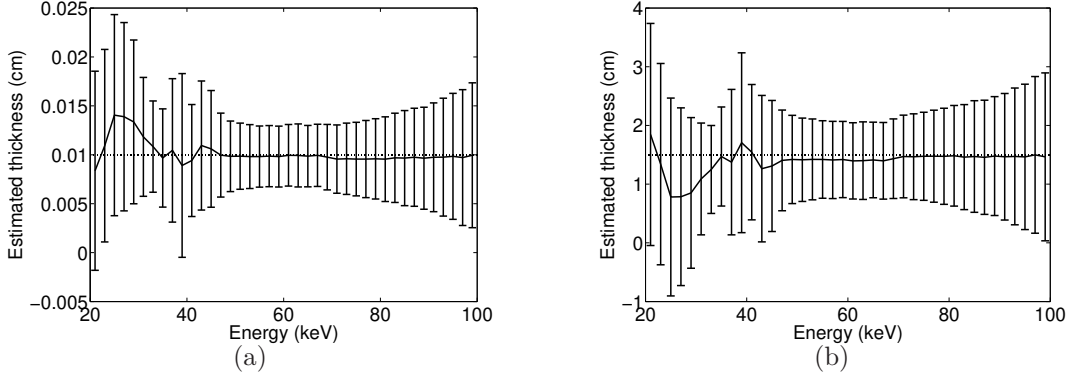


FIG. 4. Mean and standard deviation obtained for the material basis images for (a) iodine and (b) water, displayed at an interval of 2 keV. The calculation of these error bars allows the quantification of image noise and comparison with the theoretical prediction which leads to validation of the optimization of bin border energy based on our FOM. Optimal bin border energies are indicated by the smallest error bars. The average bias over 5 keV around the optimal bin border is 1.24% for (a) and 6.06% for (b).

scattered radiation.  $\text{Variance}_B$ , MSE and bias for the decomposition of 3 materials before and after scatter rejection can also be found in table I. Figure 6 and figure 7 show a comparison of  $\text{variance}_B$  to  $\text{variance}_A$  for the decomposition of two and three materials, respectively. The minimization of the combined  $\sigma^2$  in the decomposition leads to the optimization of energy bins.

The FOM curves based on (5) obtained using the BEAMnrc model largely agree with the ones obtained from the optimization algorithm. Figure 8 shows the highest FOM value given by the BEAMnrc model is 2 keV lower than the theoretical optimum at 60 keV for the decomposition of 0.01 cm iodine and 1.5 cm water. Similarly, for three materials, the highest FOM value obtained for the BEAMnrc model was located at 49 keV compared to 51 keV for the theoretical optimum. The predicted FOM values for  $\pm 2$  keV around the theoretical optimum was observed to be  $>96\%$  of the peak value for the BEAMnrc model in both cases.

## V. DISCUSSION AND CONCLUSIONS

BEAMnrc simulations allow for the optimization of material discrimination to be validated in an idealized environment. No imperfections other than the scattered radiation

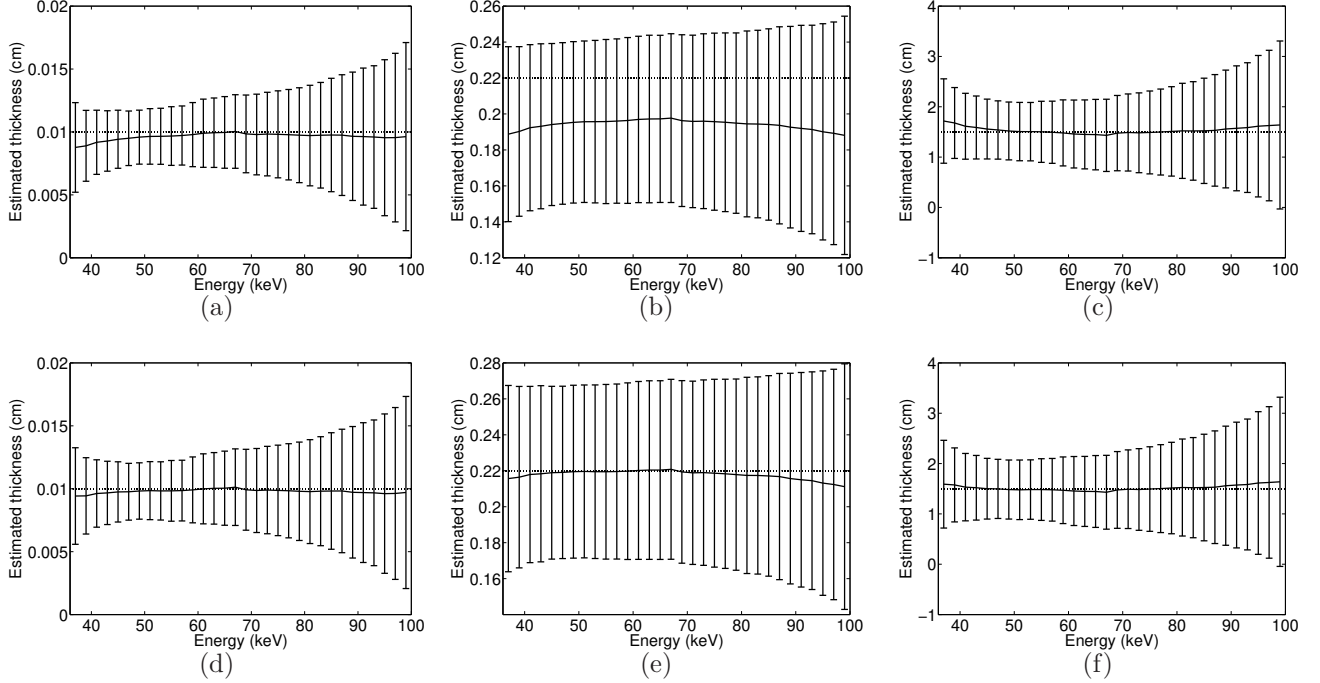


FIG. 5. Mean and standard deviation obtained for the material basis images for (a,d) iodine, (b,e) calcium and (c,f) water, displayed at an interval of 2 keVs. The average bias over 5 keV around the optimal bin border is 3.88% for (a), 11.14% for (b) and 0.91% for (c). The improvement on the bias upon the rejection of scattered radiation is shown in the lower panel. Rejection of scattered radiation improved the accuracy of material quantification, particularly in the calcium basis image (see table I). A comparison with the image noise predicted by the theoretical model is shown in figure 7 .

have been taken into account in the simulations. As shown, optimization of energy bins can provide better confidence in material thickness estimation. Given the achievable energy resolutions of the current PCDs [2, 4], we reason that the optimization algorithm [10] provides sufficient guidance for the location of energy bins when implementing material discrimination using spectral x-ray imaging.

When compared with the simulated variance, however, the theoretical prediction of image noise presents some limitations. The simulated  $\sigma^2$  incorporated both image noise sources from the projection and the open beam image. The normalization of the spatial variation in photon counts introduced a further photon counting noise inherent to the open beam image. Software limitations also precluded a better agreement between predicted and simulated variances for the decomposition of three materials, particularly for calcium. The step-wise

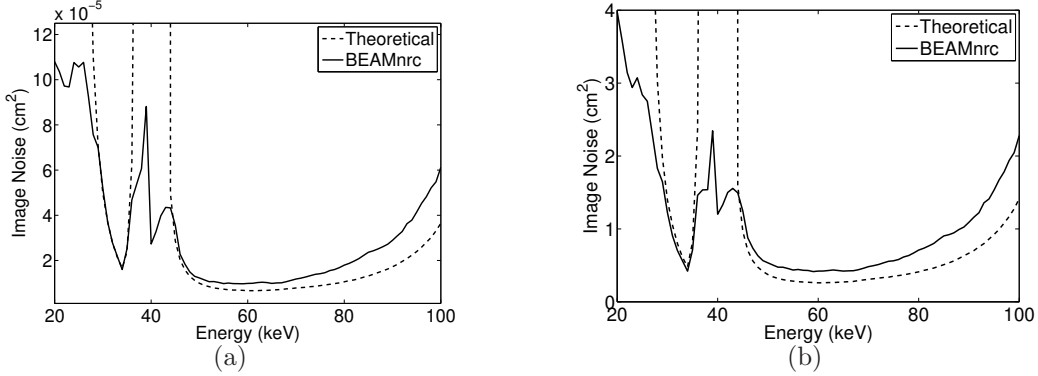


FIG. 6. Image noise of the material basis images as a function of  $E_{(h,1)}$  for (a) iodine and (b) water.  $\sigma^2$  values obtained from the theoretical model were plotted using dotted lines to show the consistency with the simulated image noise. The theoretical values were allowed to extend beyond the vertical axis to focus on the lowest  $\sigma^2$  values. An explanation of this effect will be provided in section V. A minimization of the  $\sigma^2$  values leads to the maximization of FOM and thus the optimization of energy bins.

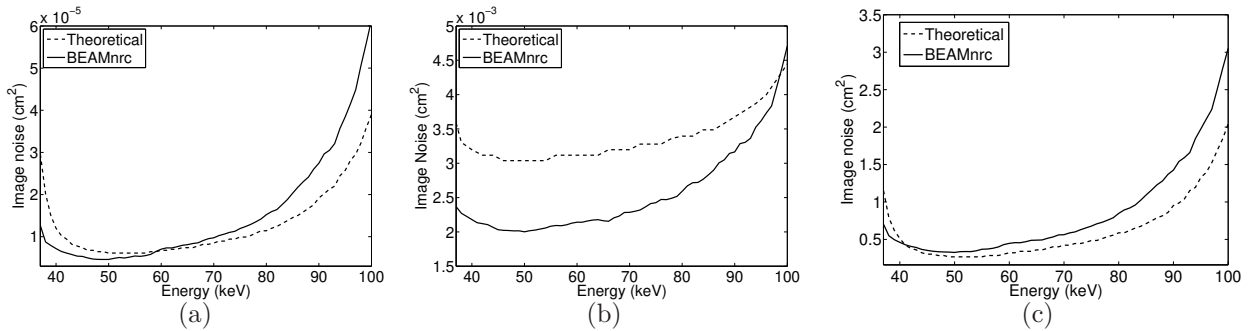


FIG. 7. Image noise of the (a) iodine, (b) calcium and (c) water basis images as a function of  $E_{(h,2)}$ . The discrepancy in (b) was due to the memory limit in Matlab, which resulted in a stepwise function for the theoretical prediction of image noise.

function in figure 7(b) is due to a limit in Matlab on the largest possible matrix size and the maximum element in an array allowed. This imposed a limit on the step size of the thickness range that could be sampled to form our confidence region, which subsequently hinders the resolution on the change of the size of the confidence region. One potential solution is to run the code on a different platform using a different version of Matlab.

For the decomposition of two materials, however, an improved agreement between the predicted and simulated  $\sigma^2$  was achieved within the limit on the largest possible matrix

TABLE I. A summary of mean square error (MSE), variance and bias obtained using the theoretical (A) and BEAMnrc (B) models.

		Materials		
		I (0.01 cm)	H <sub>2</sub> O (1.5 cm)	Ca (0.22 cm)
2 materials (2 bins)	variance <sub>A</sub> (cm <sup>2</sup> )	$6.71 \times 10^{-6}$	$2.62 \times 10^{-1}$	-
	variance <sub>B</sub> (cm <sup>2</sup> )	$9.78 \times 10^{-6}$	$4.25 \times 10^{-1}$	-
	MSE (cm <sup>2</sup> )	$9.78 \times 10^{-6}$	$4.33 \times 10^{-1}$	-
3 materials	variance <sub>A</sub> (cm <sup>2</sup> )	$6.11 \times 10^{-6}$	$2.67 \times 10^{-1}$	$3.04 \times 10^{-3}$
	variance <sub>B</sub> (cm <sup>2</sup> )	$4.82 \times 10^{-6}$	$3.33 \times 10^{-1}$	$2.02 \times 10^{-3}$
	MSE (cm <sup>2</sup> )	$4.95 \times 10^{-6}$	$3.33 \times 10^{-1}$	$2.61 \times 10^{-3}$
	Bias (%)	3.88	0.91	11.14
3 materials (Scatter rejected)	variance <sub>B</sub> (cm <sup>2</sup> )	$5.25 \times 10^{-6}$	$3.47 \times 10^{-1}$	$2.31 \times 10^{-3}$
	MSE (cm <sup>2</sup> )	$5.27 \times 10^{-6}$	$3.47 \times 10^{-1}$	$2.31 \times 10^{-3}$
	Bias (%)	1.67	1.22	0.21

size in Matlab. A dose calculation procedure, such as [33, 34], may be implemented on the theoretical model upon the validation to convert the estimated counts into e.g. mean glandular dose required to confidently decompose a calcification feature within breast tissue (see [35]). The confidence region in the theoretical model in figure 6 can expand infinitely when the counting statistics for a bin border energy is poor. The predicted image noise hence extended further than the axis, as shown in figure 6, while the simulated image noise has a finite range. Figure 9 depicts plots of the entire range of the image noise.

Although the BEAMnrc model was setup in this work to enable separate simulations of x-ray tube and transmission through the imaging object, the generation of x-ray photons was largely inefficient. Furthermore, the calculation time of the in-house Matlab code to translate phsp information into projection image increased proportionally to the number of incident particles. The pixel size on the detector plane was set to be four times that of the Medipix detector to partially compensate for these limitations. For the given imaging geometry, object size and the number of primary history, it was found that the detector pitch of 220  $\mu\text{m}$  achieved an adequate balance between simulated image resolution and spectral SNR for acceptable accuracy in thickness estimation. It should be noted that, for computational

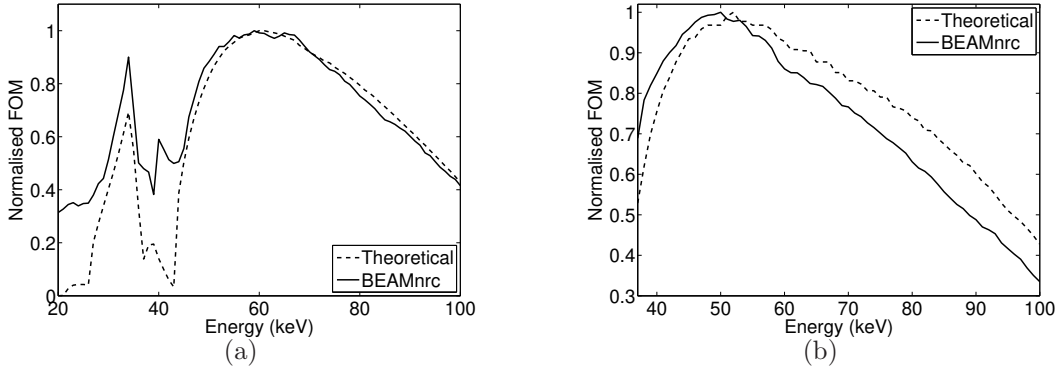


FIG. 8. Consistencies between the simulated and the theoretical optimal bin border energies. (a) The highest FOM value obtained with the BEAMnrc model differs by 2 keV from the theoretical optimum of 60 keV for the decomposition of iodine and water. (b) Likewise, for the decomposition of three materials, optimal  $E_{(h,2)}$  was located at 51 keV and 49 keV for the theoretical and the BEAMnrc simulation, respectively.

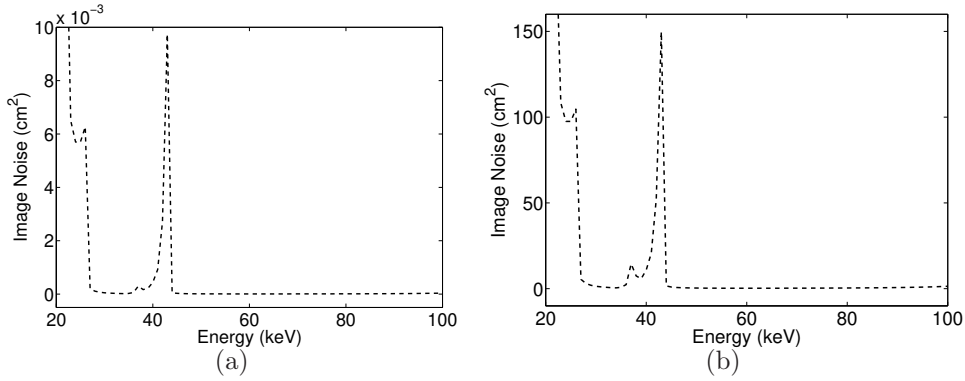


FIG. 9. While figure 6 focused on the lowest  $\sigma^2$  values for (a) iodine and (b) water at the optimal  $E_{(h,1)}$  value, the vertical axis was rescaled in this figure to show the entire range of image noise. The confidence region in the theoretical model was allowed to extend indefinitely when the photon counting statistics were poor for a bin border energy. The predicted image noise hence extended beyond the axis in figure 6.

efficiency and due to hardware limitations, the simulations were performed below the typical clinical settings of standard x-ray photon flux rates. Simulated detected counts were less than 900 per pixel for all cases. It is expected that increasing the number of detected counts can facilitate noise reduction in the simulated spectrum and thereby provide improved agreements between  $\text{variance}_A$  and  $\text{variance}_B$ . As such, spectra of smaller pixel pitches can

be simulated too.

Furthermore, the scatter contribution between 10 keV and 60 keV for the three material decomposition was 25% of the total photon counts, which contributed to the 11% bias in calcium thickness estimation in table I. The 10% scattered radiation between 10 keV and 60 keV for the decomposition of two materials does not result in a considerable bias in thickness estimation (variance  $\approx$  MSE) and was thus considered negligible. While the rejection of scattered radiation lowered the bias in the decomposition, the reduction in simulated detected photon counts resulted in a marginally higher image noise in the decomposition of three materials. The quantification and rejection of scattered radiation was enabled by the particle interaction tracking ability in BEAMnrc [21]. Note that practical implementation of scatter rejection, such as a multi-slit collimators have been implemented by other groups [36, 37]. A future application is therefore scatter correction utilizing the particle tracking function in BEAMnrc, which may help reducing the impact of scattered radiation on material decomposition using spectral x-ray imaging [38].

## ACKNOWLEDGMENTS

We gratefully acknowledge Tony Teke (BC Cancer Agency, Vancouver, Canada) for providing the initial code to read the BEAMnrc phsp files, and Dr. Vladimir Mencl and Dr. François Bissey for their help on the BlueFern<sup>®</sup> setup. SJN would like to thank Mars Bioimaging Ltd (MBI) for his PhD scholarship. RST would like to acknowledge a Study Abroad Grant from Nordeafonden in Copenhagen and the University of Canterbury summer scholarship scheme for their financial support throughout this work.

- 
- [1] P. Pangaud, S. Basolo, N. Boudet, J.-F. c. Berar, B. Chantepie, P. Delpierre, B. Dinkespiler, S. Hustache, M. Menouni, and C. Morel, *XPAD3: A new photon counting chip for x-ray CT-scanner*, *Nucl. Instrum. Methods Phys. Res. A* **571** (2007), no. 1-2 321–4.
  - [2] R. Ballabriga, M. Campbell, E. Heijne, X. Llopart, L. Tlustos, and W. Wong, *Medipix3: A 64k pixel detector readout chip working in single photon counting mode with improved spectrometric performance*, *Nuclear Instruments and Methods in Physics Research Section A*:



- Accelerators, Spectrometers, Detectors and Associated Equipment* **633** (2011) S15–8. doi: DOI: 10.1016/j.nima.2010.06.108.
- [3] M. F. Walsh, S. J. Nik, S. Procz, M. Pichotkac, S. T. Bell, R. M. N. Doesburg, N. De Ruiter, C. J. Bateman, A. I. Chernoglazove, R. K. Panta, A. P. H. Butler, and P. H. Butler, *Spectroscopic CT data acquisition with Medipix3.1*, *Journal of Instrumentation* **8** (2013), no. 10 P10012.
- [4] J. P. Schlomka, E. Roessl, R. Dorscheid, S. Dill, G. Martens, T. Istel, C. Baumer, C. Herrmann, R. Steadman, G. Zeitler, A. Livne, and R. Proksa, *Experimental feasibility of multi-energy photon-counting K-edge imaging in pre-clinical computed tomography*, *Physics in Medicine and Biology* **53** (2008), no. 15 4031.
- [5] R. E. Alvarez and A. Macovski, *Energy-selective reconstructions in x-ray computerised tomography*, *Physics in Medicine and Biology* **21** (1976), no. 5 733–744.
- [6] E. Roessl, D. Cormode, B. Brendel, K. Jrgen Engel, G. Martens, A. Thran, Z. Fayad, and R. Proksa, *Preclinical spectral computed tomography of gold nano-particles*, *Nuclear Instruments and Methods in Physics Research Section A: Accelerators, Spectrometers, Detectors and Associated Equipment* **648** (2010), no. Supplement 1.
- [7] H. Q. Le and S. Molloy, *Segmentation and quantification of materials with energy discriminating computed tomography: A phantom study*, *Medical Physics* **38** (2011) 228.
- [8] G. Beldjoudi, V. Rebuffel, L. Verger, V. Kaftandjian, and J. Rinkel, *An optimised method for material identification using a photon counting detector*, *Nuclear Instruments and Methods in Physics Research Section A: Accelerators, Spectrometers, Detectors and Associated Equipment* **663** (2011), no. 1 26–36.
- [9] E. C. Frey, X. Wang, Y. Du, K. Taguchi, J. Xu, and B. M. W. Tsui, *Investigation of the use of photon counting x-ray detectors with energy discrimination capability for material decomposition in micro-computed tomography*, *Proc. SPIE* **6510** (2007) 65100A–11.
- [10] S. J. Nik, J. Meyer, and R. Watts, *Optimal material discrimination using spectral x-ray imaging*, *Physics in Medicine and Biology* **56** (2011), no. 18 5969.
- [11] E. Roessl and R. Proksa, *K-edge imaging in x-ray computed tomography using multi-bin photon counting detectors*, *Physics in Medicine and Biology* **52** (2007), no. 15 4679.
- [12] A. S. Wang and N. J. Pelc, *Sufficient statistics as a generalization of binning in spectral x-ray imaging*, *IEEE Trans. Med. Imaging* **30** (2011), no. 1 84–93.

- [13] A. C. Rencher, *Methods of Multivariate Analysis*. Wiley Series In Probability and Mathematical Statistics. Wiley, 1995.
- [14] F. James, *Statistical methods in experimental physics*. World Scientific Publishing, Singapore, second ed., 2006.
- [15] E. Roessl, B. Brendel, K. J. Engel, J. P. Schlomka, A. Thran, and R. Proksa, *Sensitivity of photon-counting based k-edge imaging in x-ray computed tomography*, *Medical Imaging, IEEE Transactions on* **30** (2011), no. 9 1678–1690.
- [16] M. Weigel, S. V. Vollmar, and W. A. Kalender, *Spectral optimization for dedicated breast CT*, *Med. Phys.* **38** (2011), no. 1 114–124.
- [17] S. Leng, L. Yu, J. Wang, J. G. Fletcher, C. A. Mistretta, and C. H. McCollough, *Noise reduction in spectral ct: Reducing dose and breaking the trade-off between image noise and energy bin selection*, *Med. Phys.* **38** (2011), no. 9 4946.
- [18] J. Giersch, A. Weidemann, and G. Anton, *Rosi—an object-oriented and parallel-computing monte carlo simulation for x-ray imaging*, *Nuclear Instruments and Methods in Physics Research Section A: Accelerators, Spectrometers, Detectors and Associated Equipment* **509** (2003), no. 1-3 151–156.
- [19] J. Ducote and S. Molloy, *Quantification of breast density with dual energy mammography: A simulation study*, *Med. Phys.* **35** (2008), no. 12 5411.
- [20] D. W. O. Rogers, B. A. Faddegon, G. X. Ding, C. M. Ma, J. We, and T. R. Mackie, *BEAM: A Monte Carlo code to simulate radiotherapy treatment units*, *Med. Phys.* **22** (1995), no. 5 503–24.
- [21] D. W. O. Rogers, B. R. Walters, and I. Kawrakow, *BEAMnrc users manual*, *NRC Report PIRS-0509(A)revK* (2004).
- [22] B. E. Currie, *Monte carlo investigation into superficial cancer treatments of the head and neck*, Master’s thesis, Department of Physics and Astronomy, University of Canterbury, Christchurch, New Zealand, 2007.
- [23] R. S. et al., *Thing, A Virtual Spectral CT scanner*, *Australasian Physical & Engineering Sciences in Medicine* **34** (2011) 123–124.
- [24] I. Kawrakow, E. Mainegra-Hing, D. Rogers, F. Tessier, and B. Walters, *The egsnrc code system: Monte carlo simulation of electron and photon transport*, *NRCC Report PIRS-701* (2011).

- [25] D. W. O. Rogers, *Fifty years of monte carlo simulations for medical physics*, *Physics in Medicine and Biology* **51** (2006), no. 13 R287.
- [26] M. F. Walsh, A. M. T. Opie, J. P. Ronaldson, R. M. N. Doesburg, S. J. Nik, J. L. Mohr, R. Ballabriga, A. P. H. Butler, and P. H. Butler, *First CT using Medipix3 and the MARS-CT-3 spectral scanner*, *Journal of Instrumentation* **6** (2011a), no. 01 C01095.
- [27] C.-M. Ma and D. W. O. Rogers, *BEAMDP as a General-Purpose Utility*, *NRC Report PIRS-0509(E)revA* (2009).
- [28] R. E. Alvarez, *Estimator for photon counting energy selective x-ray imaging with multibin pulse height analysis*, *Medical Physics* **38** (2011), no. 5 2324–2334.
- [29] C. Lagarias, Jeffrey, A. Reeds, James, H. Wright, Margaret, and E. Wright, Paul, *Convergence properties of the Nelder–Mead simplex method in low dimensions*, *SIAM Journal on Optimization* **9** (1998), no. 1 112–147.
- [30] A. Rose, *A unified approach to the performance of photographic film, television pickup tubes, and the human eye*, *Journal of the Society of Motion Picture Engineers* **47** (1946), no. 4 273–294.
- [31] J. Ducote, Y. Alivov, and S. Molloy, *Imaging of nanoparticles with dual-energy computed tomography*, *Physics in Medicine and Biology* **56** (2011), no. 7 2031–2044.
- [32] T. Slovis, *Children, computed tomography radiation dose, and the As Low As Reasonably Achievable (ALARA) concept*, *Pediatrics* **112** (2003), no. 4 971–972.
- [33] J. M. Boone, *Normalized glandular dose (DgN) coefficients for arbitrary x-ray spectra in mammography: Computer-fit values of Monte Carlo derived data*, *Medical Physics* **29** (2002), no. 5 869–875.
- [34] J. M. Boone and J. A. Seibert, *An accurate method for computer-generating tungsten anode x-ray spectra from 30 to 140 kV*, *Medical Physics* **24** (1997), no. 11 1661–1670.
- [35] S. J. Nik, *Optimising the benefits of spectral x-ray imaging in material decomposition*. PhD thesis, Department of Physics and Astronomy, University of Canterbury, Christchurch, New Zealand, 2013.
- [36] H. Ding and S. Molloy, *Quantification of breast density with spectral mammography based on a scanned multi-slit photon-counting detector: a feasibility study*, *Physics in Medicine and Biology* **57** (2012), no. 15 4719–4738.

- [37] P. M. Shikhaliev, *Computed tomography with energy-resolved detection: a feasibility study*, *Physics in Medicine and Biology* **53** (2008), no. 5 1475–1495.
- [38] J. Wiegert, K. J. Engel, and C. Herrmann, *Impact of scattered radiation on spectral ct*, in *Medical Imaging 2009: Physics of Medical Imaging*, vol. 7258, (Lake Buena Vista, FL, USA), pp. 72583X–10, SPIE, 2009.